Supplementary Materials

"*Selectivity Mechanism of the Nuclear Pore Complex Characterized by Single Cargo Tracking*"

Movie S1 | Example of imported QDs after 20 minutes. A typical movie showing imported QDs in a single nucleus after 20 minutes of import. 2 QDs are seen to diffuse inside the confined volume of the cell nucleus. The fitted outline of the nuclear envelope taken from a brightfield image taken immediately after this movie is overlaid in green. (File: MovieS1.avi)

Movie S2 | Example of importing single QD. An example of single QD cargo successfully translocating through a NPC. The nuclear envelope bisects the field of view, running from top to bottom. The QD is observed arriving from the cytoplasm (left), residing at the NPC, and then leaving into the nucleus (right). (File: MovieS2.avi)

1. PROTEIN EXPRESSION AND PURIFICATION

Plasmid	Description	Resistance	Source
Importin-β	His_6 – Importin-β	Kanamycin	Steven Adam
Ran	His_6 - Ran	Kanamycin	Kalab *et al.*[1]
IBB	His_6 – SnpIBB – Z – Cys - Cys	Kanamycin	This study
S-peptide	His_6 – S-peptide – Z – Cys - Cys	Kanamycin	This study
IBB-Cerulean	His_6 – SnpIBB – Cerulean - Biotin	Ampicillin	This study
Biotin ligase	Untagged BirA	Chloramphenicol	Avidity Inc.

NTF2 was purchased from Sigma-Aldrich. All other proteins were expressed and purified as described below. *E. coli* (BL21 DE3) were transformed with the appropriate plasmid and a small number of colonies were picked from the plate into flasks containing 1 l of LB medium plus the appropriate antibiotic. Biotinylated proteins were expressed in the presence of biotin (stock: 100 mM biotin, pH 11; 1 ml per 1L culture) and a biotin ligase. The cells were grown at 37 °C to A600 of 0.6 and then induced with 0.5 mM IPTG overnight. Cells were harvested by centrifugation at 5000 g at 4 °C for 15 min and the pellet was resuspended in phosphate buffer (pH 7.4) containing 0.5 M NaCl, 20 mM imidazole, 1 mM β-mercaptoethanol and protease inhibitors. Proteins were initially purified by Ni-NTA affinity chromatography, followed by size-exclusion chromatography (Superdex 75, Amersham Pharmacia). Proteins were typically dialysed into XB buffer (10 mM HEPES pH 7.7, 1 mM $MgCl_2$, 100 mM KCl, 50 mM sucrose), flash frozen in liquid nitrogen and stored at -80 °C. Protein purity was judged by SDS-PAGE, and concentrations determined by UV absorbance (using calculated extinction coefficients) or Bradford assays. Nucleotide loading of Ran was performed as described previously[2]. Briefly, the protein was incubated for 40 min on ice with 6 mM EDTA and a 50 fold excess of nucleotide. The reaction was stopped with a final concentration of 25 mM $MgCl_2$, added slowly. The protein was then dialysed against 30 mM potassium phosphate pH7.6, including 2 mM Mg-acetate, 2 mM GDP, 7% glycerol and 2 mM β-mercaptoethanol, at 4 °C overnight.

Labelling of proteins with fluorescent dyes. Proteins containing engineered cysteine residues were labelled with maleimide functionalised DyLight 549 (Pierce) as per the manufacturers instructions. Excess uncoupled dye was removed by dialysis, prior to use.

2. QD CARGO SYNTHESIS AND CHARACTERISATION

QD cargo synthesis. Numerous labelling strategies and chemistries were tried to create a small, stable and transport functional cargo. The one successful strategy is based on amino PEG functionalised QDs coupled to the snurportin-IBB. Amino PEG functionalised QDs, with an emission peak of 605 nm, were acquired from Invitrogen. A two-step conjugation reaction was used. QDs were first coupled to Sulfosuccinimidyl-4-(*N*-maleimidomethyl)cyclohexane-1-carboxylate (SulfoSMCC) in standard PBS. Excess SulfoSMCC was removed via spin filtration. Activated QDs were then coupled to cysteine-terminated recombinant protein in PBS supplemented with 350mM NaCl and 2mM EDTA. Uncoupled protein was removed by a second round of spin-filtration. The mean hydrodynamic diameter of QD cargos was determined by dynamic light scattering (see below).

Large cargo synthesis. Larger QD cargos were created using Streptavidin conjugated 605 nm QDs (Invitrogen) coupled to a biotinylated Snurportin IBB-Cerulean. QDs were conjugated to the protein construct for 15 mins on ice prior to use. The mean hydrodynamic diameter of QD cargos was determined by dynamic light scattering (see below).

Dynamic Light Scattering (DLS) measurements of QD cargo size. DLS measurements were performed on a Malvern Zetasizer Nano to measure the hydrodynamic radius. QD cargos were diluted to a final concentration of 8-10 nM in Transport buffer (20 mM HEPES, 110 mM KOAc, 5 mM NaOAc, 2mM MgOAc, 2 mM DTT, pH 7.3) and filtered (0.1 μm) to remove any aggregates. This concentration range yielded the best quality of data as judged by the polydispersity index (PDI). Measurements of the cargo in complex were performed in the presence of 3.8 or 1.0 μM importin β. In samples measured in the presence of importin β, the free importin β peak was found to be 10.6 ± 1.8nm, only slightly larger than the known size from the crystal structure[3,4,5].

Count rates were typically above 200 kcps and multiple repeat measurements were taken. Data were analysed using the Malvern software, using the Multiple Narrow Bands fitting algorithm and Refractive Index and Absorption settings for proteins (RI = 1.45, A = 0.001). While the material properties of our cargo are likely to be different from those of protein, the effect of reprocessing the data using material properties more consistent with the nanocrystal core of QDots (RI = 3.0, A = 0.1) resulted in diameters only 0.1nm different than using the protein settings.

Table S1| Hydrodynamic diameters of the QD cargos with and without importin-β.

	- Imp β	+ Imp β	Δd
QD605 – NH_2	16.0 ± 4.1		
QD605 - Protein	17.8 ± 4.3	30.2 ± 6.2	12.4 (6.3 nm / β)
QD605 - Streptavidin	18.2 ± 4.6		
QD605 – Streptavidin - Protein	22.6 ± 6.3	40.9 ± 8.7	18.3 (9.15 nm / β)

Calculation of maximum number of importin-βs bound per QD cargo. The change in diameter upon saturated binding of importin β allows us to estimate the number of importin β proteins bound per QD cargo. The approximate volume of importin β was calculated to be ~300nm^3 from the crystal structure. The change in volume upon importin β binding divided by the volume of Importin β gives ~38 copies / QD. As a second calculation, the crystal structure of importin β bound to the Snurportin-1 IBB shows that the protein has an approximate footprint of ~ 26nm^2. The surface area of the QD-IBB in the absence of importin β can also accommodate approximately 38 proteins. The outer footprint of importin β is calculated to be approximately 56nm^2. The surface area in the presence of Importin β could accommodate ~51 copies. Combining these calculations, we estimate the number of importin βs bound per QD to be ~40.

3. IMPORT ASSAYS

Buffers used:

- PBS (137 mM NaCl, 2.7 mM KCl, 8 mM Na2HPO4, 2 mM KH2PO4, pH 7.4)
- Permeabilisation buffer (50 mM HEPES, 50 mM KOAc, 8 mM MgCl2, pH 7.3)
- Transport Buffer (20 mM HEPES, 110 mM KOAc, 5 mM NaOAc, 2mM MgOAc, 2 mM DTT, pH 7.3).

HeLa cells were cultured in DMEM media (Gibco) and plated on glass bottomed (size 0 thickness) poly-lysine coated chambers (Mattek Corp.). Cells were permeabilised according to the following protocol. The chambers were washed for 3 x 5 min with PBS, followed by a 2 min wash with permeabilisation buffer, followed by a 10 min permeabilisation with digitonin (50 mg) in permeabilisation buffer. Digitonin was subsequently removed by washing for 3 x 5 min with transport buffer. After the final wash, excess liquid was wicked off and a transport mix containing the QD probe and the recombinant import system was quickly added. Control experiments with fluorescently (FITC) labelled dextrans (70 kDa) were used to confirm that the nuclear envelope remained intact following the digitonin permeabilisation. The final transport mix (100 µl) contained 50 pM QD, 0.5 µM importin β, 4 µM RanGDP, 1 µM NTF2, and 1 mM GTP in transport buffer. Once the transport mix had been added, the chamber was allowed to settle before imaging began.

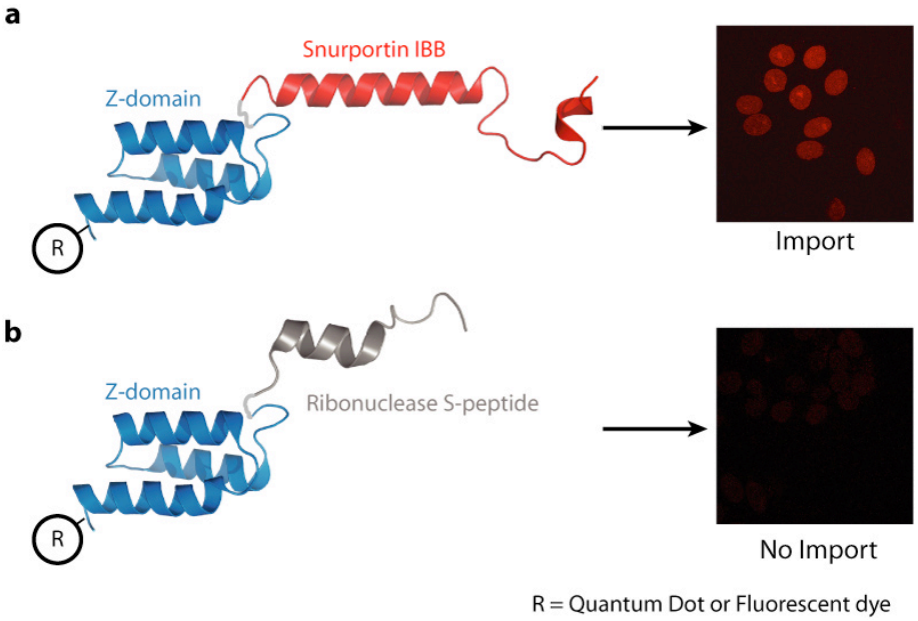

Figure S1 | Import of fluorescent dye labelled protein in HeLa cells using recombinant import system. (**a**) The IBB-Z-CysCys cargo protein labelled with maleimide DyLight 549 in the presence of the recombinant import system after 15 minutes of import. (**b**) No import is observed for the S-peptide variant.

Since the overall transport efficiency of QD cargo import is low, we optimised the transport conditions using the fluorescently labelled IBB fusion protein and standard confocal microscopy (Fig S1). Subsequently, we confirmed QD

cargo import by visual inspection of single molecule fluorescence movies rather than still images. Supplementary movies S1 and S2 show QDs inside the nucleus moving and bounded by the nuclear envelope.

4. IMAGING

Single molecule fluorescence (SMF) microscopy. The microscope was based on a Nikon TE-2000 total internal reflection fluorescence (TIRF) microscope. A beam from a solid-state continuous-wave laser (532 nm, 100 mW, Coherent Compass 315M-100) was passed through a λ/4 plate to circularly polarize the light, a beam expander to enlarge the illumination area, and steered through free space to the microscope using a gimbal mirror mounted on a translation stage. The beam was focussed on the back focal plane of a high-NA objective (Apo 100x NA1.65, Olympus). The illumination beam was angled at just above the critical angle for TIR, passing at a shallow angle through the cells[6]. This configuration allows high signal to noise movies to be recorded at a greater depth into the sample than conventional TIRF. Typical power at the objective was 10mW. Optical filters: a dichroic mirror and emission filter were used. A micrometer stage (Semprex) with piezo controlled nanopositioner (Mad City Labs) was used to position the cells. Movies were captured using a cooled electron multiplying CCD camera (Andor iXon+) running at 40 Hz at -78 °C. All instrumentation was controlled using custom C++ code. Image scaling was determined using a stage micrometer (SPI; 10 μm divisions), yielding a single pixel of dimensions 144.5 x 144.5 nm.

Confocal microscopy was performed using a Zeiss 510 Axiovert (an inverted confocal microscope with Zeiss LSM scanhead) with excitation from a 488nm Argon-ion or 549nm He-Ne laser. QD fluorescence was viewed with 560LP dichroic.

5. TRAJECTORY ANALYSIS, QUALITY METRICS, AND MAGNITUDES OF VARIOUS ERRORS

This section is a detailed description of how the data were analyzed, including, where applicable, a very detailed discussion of methodological advantages, particularities, and limitations. We first provide a brief summary of our error sources and their magnitudes. Of note, by far the largest source of error/uncertainty in our experiments is the precision with which the QD can be localized. This depends on many factors including the number of photons collected from the QD (and the heterogeneity in the QD quantum yield), the background image noise, and QD blinking.

Type of error or limitation	Data affected by error or limitation	Estimated/Measured Magnitude	See SM Page
Limited photons; QD Localisation precision	All data	6 nm per single frame	6
Stage drift	All data	11 nm / min; ~6 nm per trajectory	7
Rotational uncertainty	Splitting of the diffusion coefficient into transverse and parallel components, Fig. 3f	0.11 radians per trajectory	9
Trajectory alignment error	All averages, such as the mean size of the central channel and histograms in Fig. 2c-e	1 nm per trajectory	10
Nuclear envelope (NE) localisation	None – used to discard from analysis QDs far from the NE.	Localisation precision, ±125 nm Localisation reproducibility: ± 30 nm (brightfield) Localisation reproducibility: ± 43 nm (fluorescense)	8

OVERVIEW OF DATA ACQUISITION, PROCESSING AND ANALYSIS WORKFLOW:

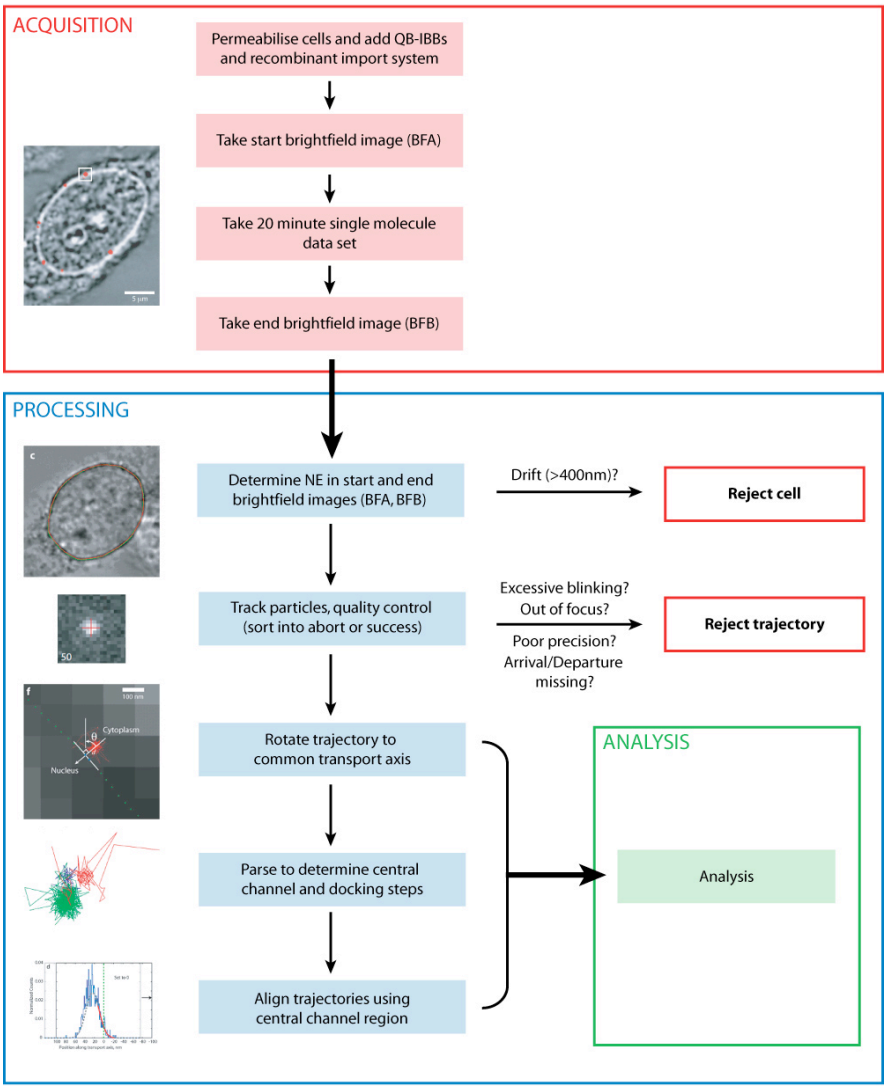

5.1 LOCALISATION PRECISION & PARTICLE TRACKING

Image analysis and particle tracking were performed using custom MATLAB code. For a sub-wavelength diameter particle, Gaussian fitting of the point spread function (PSF) yields the highest accuracy and precision of localisation[7]. Each PSF was fitted to a 2D Gaussian function:

$$f(x,y) = Ae^{-\left(\frac{(x-x_0)^2}{2\sigma_x^2}+\frac{(y-y_0)^2}{2\sigma_y^2}\right)} + B$$

where *A* is the amplitude, *B* is the background, x_0 and y_0 are the mean x and y positions, and σ_x and σ_y are the standard deviations in x and y. Since the core of the QD-IBB cargo is the single fluorescence source, the centroid determined from the PSF refers directly to the geometric centre of the entire cargo. These centroids (x_0,y_0), from each frame of the movie, were assembled into trajectories using the diffusional probability method of Crocker & Grier[8].

Localisation precision. The localisation precision of our instrument refers to how precisely we can define the centre of the PSF, given the magnification and signal to noise ratio of the image. We experimentally determined the localisation precision by immobilising QDs on to a glass coverslip and imaging the particles over time. QDs adhere to the glass surface through non-specific electrostatic interactions. The localisation precision is defined as the standard deviation of the positional distribution (σ_{xy}) of this particle. For each QD movie, we also determine the signal to noise ratio, a measurement of the quality of the image:

$$S/N = \frac{I_0 - I_b}{\sqrt{\sigma_0 \sigma_b}}$$

where I_0 and I_b are the intensities of the QD and background signal respectively, and σ_0 and σ_b are the standard deviations in the intensity of the QD and background signals[9]. The relationship between signal to noise and localisation precision for our instrument is shown below in Fig S2. Subsequently, the signal to noise ratio of each individual NPC interaction event was used to estimate its mean localisation precision. The mean localisation precision for our experiment is 6 nm, with a practical range for the dataset of 5-8 nm.

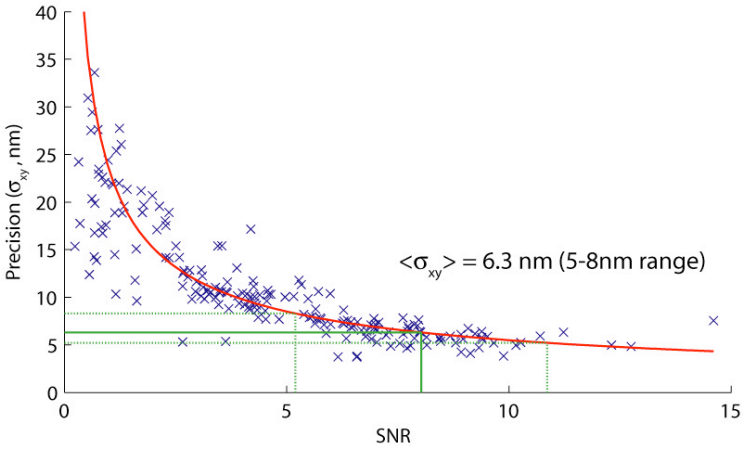

Figure S2 | Localisation precision. Multiple measurements of the position of single immobilized QDs were used to determine the precision. The SNR was calculated for each QD. The red line is a fit to a power law enabling estimation of the mean localisation precision. The solid green represents the mean SNR of the high quality trajectory data, with the spread estimated by the dashed green lines. The fit yields a mean localisation precision of 6 nm with a practical range of 5-8 nm for the experiment.

5.2 MAGNITUDE OF THERMAL DRIFT

In addition to QD localisation precision, it is also important to quantify the sample drift that occurs during the experiment. If the sample drifts during the experiment, this drift will degrade our ability to extract the true QD-position versus time trajectories. Sample drift was minimized by experimental design: (a) the sample was held by a type of micrometer stage that we have empirically found to exhibit low drift (Semprex KM series micrometer stage), (b) the micrometer stage was allowed to stabilize for several minutes after adjustment or contact, (c) the experiment was performed in a dedicated room, with no people leaving or entering immediately before or during experiment, and (d) the temperature in room was maintained within ±0.1ºC of the setpoint by a "passive" cooling system (in which air at a constant temperature is forced through the room at a constant rate through a diffuser near the floor).

We quantified drift of the sample/stage over time by tracking 40 nm and 100 nm gold nanoparticles immobilised onto the same poly-lysine coated glass Mattek chambers used for import experiments. The gold fiducial markers were imaged continuously and their position determined over time via fitting of the PSF as in section 5.1. The change in position over time is shown in Fig S3. Drift was unidirectional in each chamber, although the direction differed between chambers. The mean drift rate was 11 nm/minute (1.8 Angstrom per second).

Since all trajectories used in the detailed trajectory analysis described in the main text were < 1 minute in duration (median time 34s), we estimate that total error due to drift, for an entire trajectory, is on average about 6 nm, or on order of the localisation precision of the QD within one frame. Since the thermal drift is small compared to the scale of an entire trajectory, we did not attempt to correct for thermal drift (other than minimizing it via experimental design, see above). Consistent with the drift measurement shown in Fig S3, none of the "high precision" trajectories used in the manuscript showed any detectable net movement in the transverse axis (example shown in Fig S8b), confirming that sample drift is not a significant component of our reported cargo trajectories.

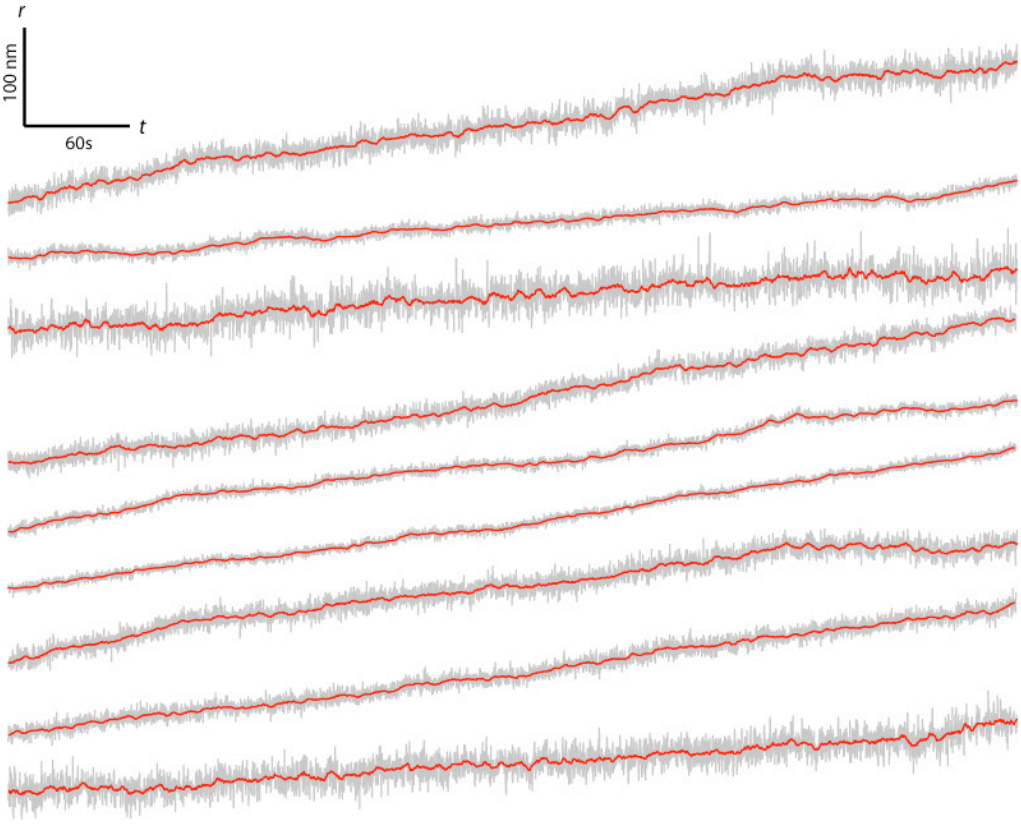

Figure S3 | Stage/sample drift. Each trace represents the displacement (change in position, r_t-r_0) over time (t) of a single fiducial marker. Raw positional data are shown in gray and the running mean (2 s filter) in red. The scale is shown in the top left corner.

5.3 FIRST-PASS SELECTION OF TRAJECTORIES

As described below, we used brightfield images to estimate the nuclear envelope centre line. Having an estimate of the NE centre line allowed us to discard QDs in the field of view that were far (> ± 200 nm) away from the NE, and thus could not have been interacting with an NPC. Also, the NE centre line estimate allows us to quickly assign QDs to the outside or inside of the nucleus. Finally, the NE centre line estimate allows us to "rotate" trajectories to a common frame, for ease of display (e.g. Fig 2a), generation of aggregate data such as the contour plots (Fig 2b), and for determining the parallel and transverse diffusion coefficients of Fig 3f (see also **section 5.4**).

Determining the NE centre line. Brightfield images of the nucleus were taken at the beginning and end of each experiment. The sub-pixel determination of the NE position was achieved as follows. A starting estimate was manually generated by tracing the NE in the brightfield image. Along each vector of this initial estimate, multiple 1D Gaussian curves were fitted to the intensity profile of the image along the normal to the estimate axis. The fitting yields estimates of the centre points of the NE. This process was repeated with multiple, automatically generated variations of the initial starting estimate of the NE. The final NE was generated using a bi-dimensional running mean filter on all found points. The NE was always defined as a series of consecutive vectors in the clockwise direction, allowing subsequent rotation of the trajectories and the preservation of the cytoplasm-nucleus vector.

The advantages and limitations of using the brightfield image to locate and define the NE were investigated with several different fluorescent markers for the NE or NPC (Fig S4) and subsequent cross-comparison of the positions of the NE found from each image. Typically, the positions of points in the NE determined from brightfield images and fluorescence images (using YFP-imp-β as an NE marker) were within 70 nm of one another. Equivalent results are obtained using other NE markers, such as QD-IBB (+importin-β, -Ran) or the fluorescent membrane dye FM4-64.

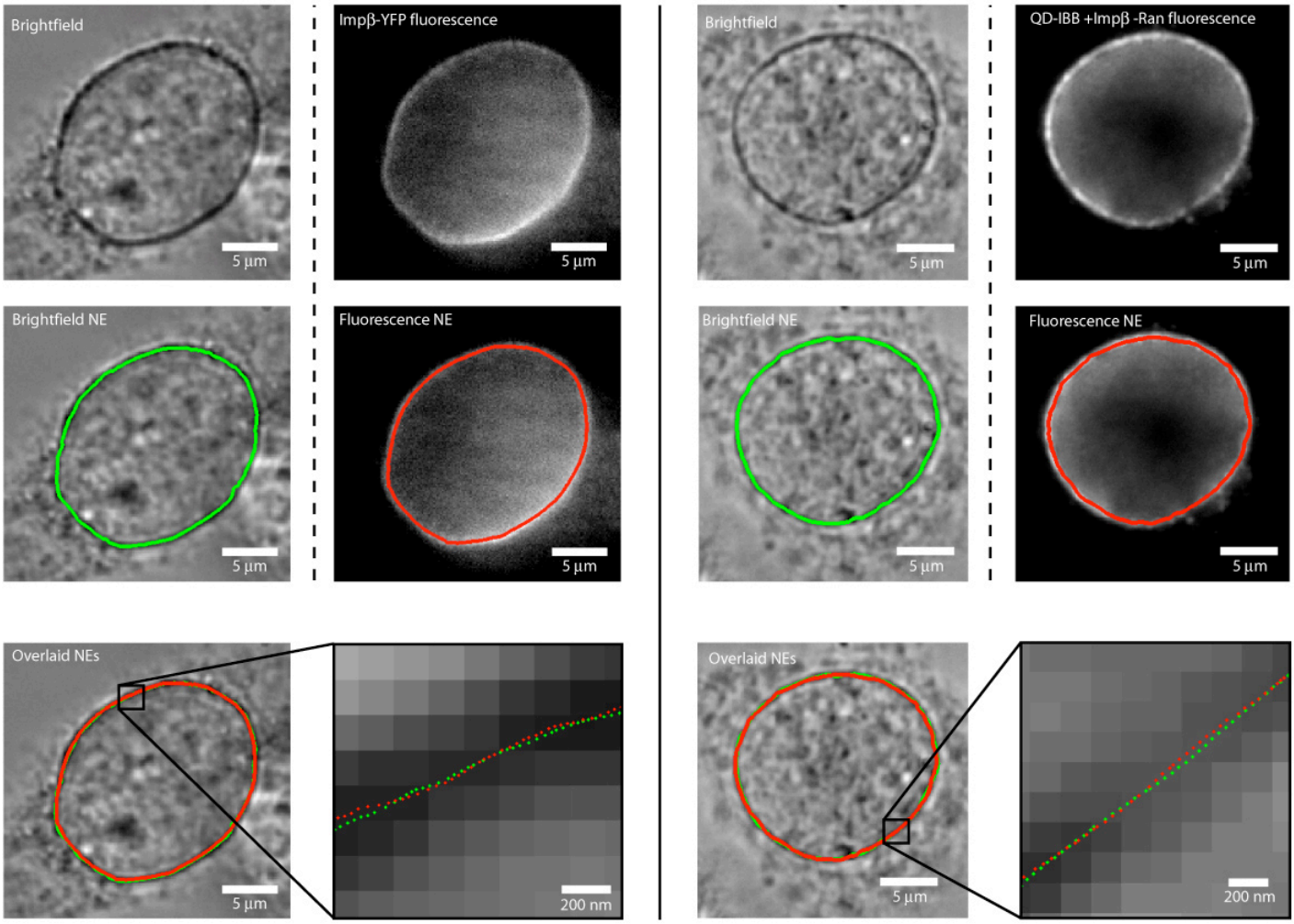

Figure S4 | Nuclear Envelope (NE) localisation. (left) Brightfield image of the nucleus of a cell showing the found NE overlaid in green. Also shown is a fluorescence image of the same nucleus (now with importin-β-YFP labelling individual NPCs) showing the NE determined from this image in red. At the bottom is the brightfield image with the found NE envelopes from brightfield (green) and fluorescence (red) and a region showing the differences between the positions of points on the NE. The typical difference is less than 70 nm (right) with QD-IBB (+imp-β -Ran) as a marker for the NE. Similar results are obtained when using other NE markers such as the FM4-64 membrane dye.

We assessed the reproducibility of this method of determining the NE by repeatedly (n = 10) tracing the same nucleus in brightfield or fluorescence images and determining the variation in estimated envelope positions (Fig S5). The mean deviation from the mean envelope position was 30 nm (median 24 nm) for brightfield images and 43 nm (median 35 nm) for fluorescence images of the same cell (Fig S5).

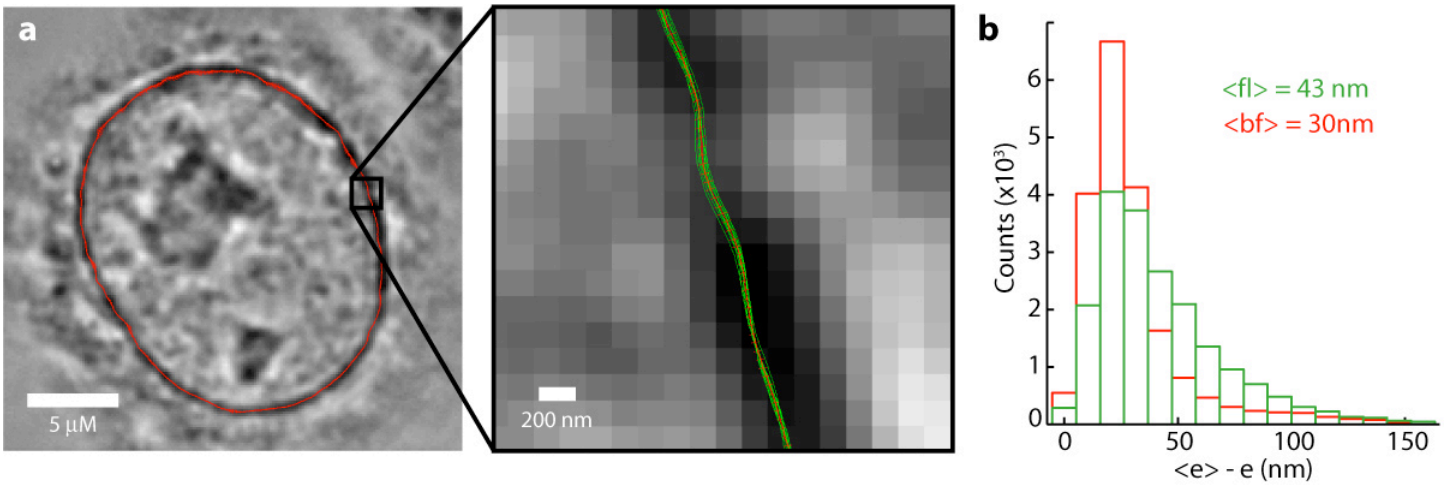

Figure S5 | Reproducibility of the NE bulk fitting procedure. (**a**) Multiple tracings (n=10) of the brightfield or fluorescence image yield the spread in found envelope positions. The width of the red line represents 3σ from the mean envelope position. The centre panel shows an expanded region of the envelope with individual NE fits in green and the mean envelope position in red. (**b**) Histogram of the deviation from the mean envelope position for brightfield (red) and fluorescence (green) images.

5.4 ROTATION OF TRAJECTORIES TO A COMMON FRAME

For ease of display, calculation of mean channel dimensions, and splitting of the diffusion coefficients into parallel and transverse components, we rotated the trajectories to a common frame. Otherwise, for example, in some figures an import event would feature the cargo moving left to right, and in other figures, it might move from top-to-bottom, and so forth. We denote the common transport axis as ***X*** (method in Fig S6). This common axis has the cytoplasm to nucleus vector pointing downward (Fig S6), and thus in all figures in the main text the cytoplasm is on the top of the panel, and the nuclear interior is on the bottom.

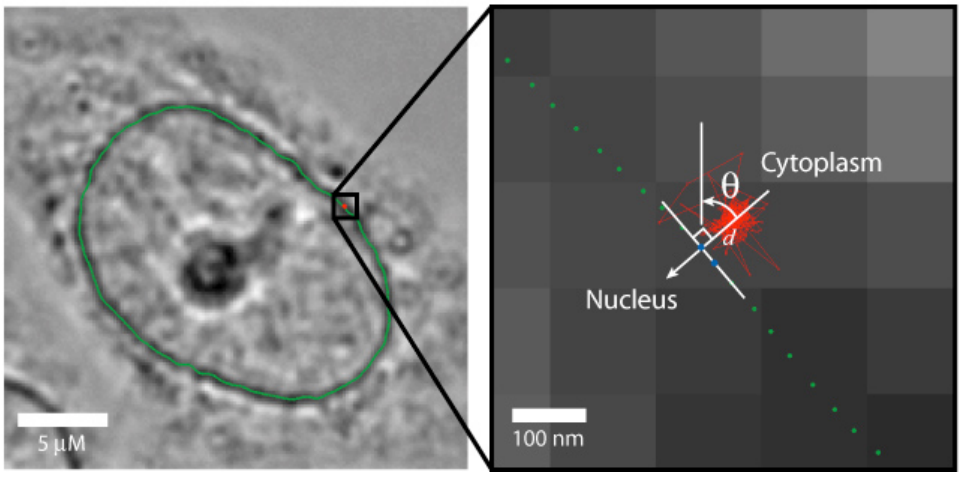

Figure S6 | Rotation of trajectories to a common transport axis. (**left**) Brightfield image with NE and single molecule QD import trajectory overlaid. The region in the black box is expanded in the next panel. (**right**) The trajectory is rotated by first selecting the two closest NE points (blue dots) to the centre of the trajectory. The distance *d*, is used to filter trajectories and select only those within a defined distance threshold (200 nm). Next, the trajectory is rotated by the angle θ; this is defined as the angle between the normal to the tangent of the envelope (i.e. the normal to the line through the two blue dots) and the vertical. All trajectories are rotated such that pore axis vector direction is preserved (cytoplasm at top, nucleus at bottom).

As shown in Fig S4, using the NE determined from the brightfield images introduces angular uncertainties. To estimate the rotational uncertainty introduced by our NE determination method we compared the NE positions found from fitting the brightfield and fluorescence images of the NE from multiple cells. An analysis of the angular difference between equivalent segments of the NE from brightfield or fluorescence images shows that trajectories are likely to have a rotational uncertainty of not more than 6º (0.11 radians, Fig S7). This uncertainty in the angle of rotation would result in an apparent compaction or elongation of the trajectory along the transport axis of less than 1%.

Figure S7 | Estimation of uncertainty in trajectory rotation arising from NE determination. Each segment of the found NE determined from brightfield (red ⊥) and fluorescence (green ⊥) images of cells are compared and the angular difference (θ) between them computed. The median difference is 6° (0.11 radians). Lower inset: the transport axis (black) showing ±6° variation (gray).

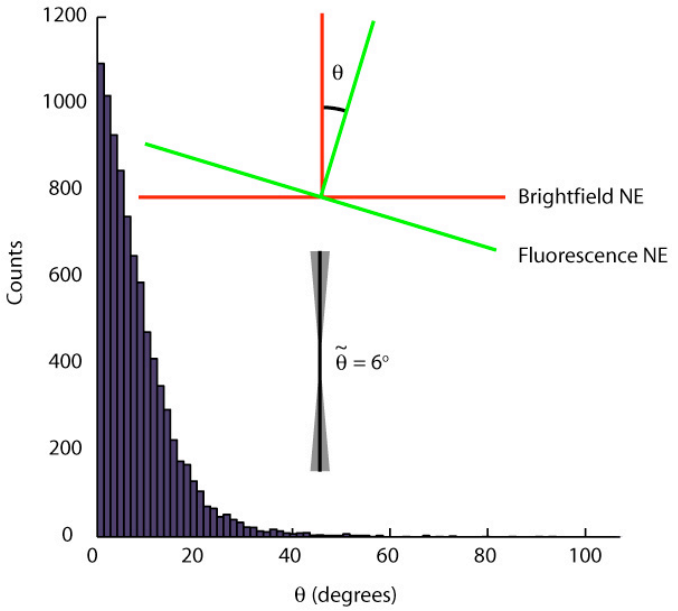

5.5 TRAJECTORY SELECTION

We performed a series of quality control steps on our single molecule trajectories to remove as many sources of potential error as possible. Movies of each particle were visually inspected to ensure that the particle was in the focal plane and that, most importantly, *both* the arrival and departure at the NE were captured. During this step, we also ensured that the particle was well separated from other particles for the entire movie that might compromise the found location of the particle. Trajectories of poorer precision (worse than 10nm) were also eliminated from our analysis. After each trajectory was rotated to the common transport axis, we inspected the trajectory for axial and lateral movements in the NPC vs. time. Trajectories were eliminated if there were any significant gaps in the trajectory, originating from QD blinking.

5.6 TRAJECTORY ALIGNMENT

To enable calculation of average properties (such a average channel dimension) and also to generate the histograms shown in the main text in Fig 2c-e, we aligned trajectories to each other, based on shared features. As discussed in the main text, all of our high-quality trajectories share several features, most prominently, the 'central channel' region featuring slow cargo velocities and characteristic values of x and y fluctuations.

Step 1 was to delineate the central channel. We began by assuming the entire trajectory was in the central channel region. Docking steps were identified if there appeared to be a region at the beginning of the trajectory that was spatially separated and there was a significant step observed in the position along the NPC axis vs. time or the position across the NPC axis vs. time (Fig. S8). Similarly, undocking steps were identified if such a region was evident at the end of the trajectory. We often observed a short series of large steps at the beginning or end of the trajectory. These data points were taken to be the QD cargo as it diffused away from the NPC and were likewise segregated out, but not included in the docking or undocking regions.

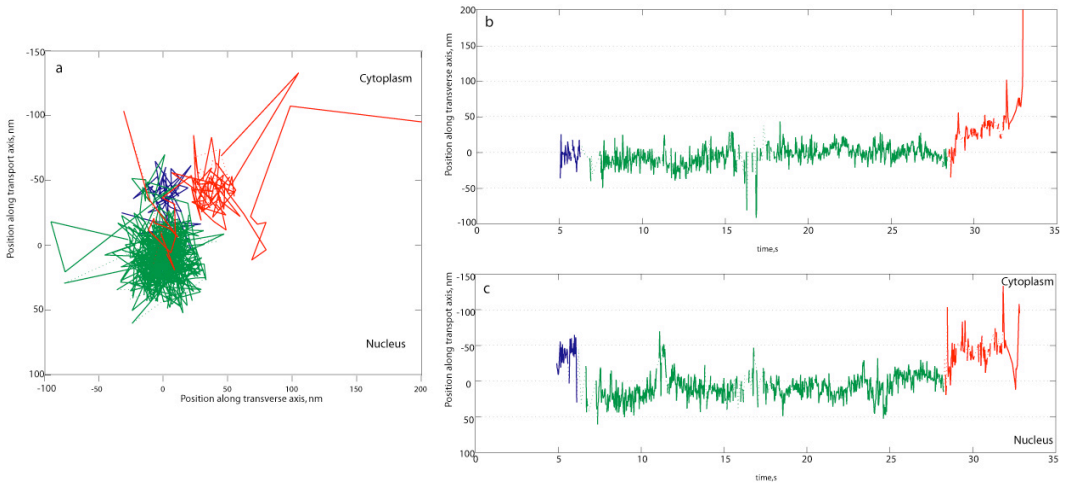

Figure S8 | Selection of the central channel region for an example trajectory. (**a**) Spatial position of a sample trajectory (cytoplasm on top, nucleus on bottom), (**b**) position along the transverse axis (parallel to the nuclear envelope) vs. time, (**c**) position along the NPC transport axis vs. time. For all panels, the docking region is coloured in blue, the central channel region in green and the undocking region in red.

Step 2. Having delineated the central channel region, we aligned the trajectories to the "front" of the central channel. We constructed a dwell-time histogram (bin width 1 nm) for each of the trajectories and then aligned it to our transport axis ***X*** by defining the cytoplasmic edge of the dwell time histogram as the zero. A Gaussian distribution was fit to the cytoplasmic edge, from 1 to 2 standard deviations and the zero point is set to 1.64 standard deviations, the point at which 95% of the data is positive.

The 'jitter' present within each dwell-time histogram limits the precision attainable with this method to about 1 nm, based on simulations done in MATLAB where we generated distributions with known origin and with the experimentally measured noise and then aligned them with our procedure. As expected, the precision of alignment increased with more data points. The precision improved from ~1.2 nm to 0.5 nm when the number of data points was increased from 100 to 300. The typical number of data points used in the data presented in the paper was between 350 and 500, and we therefore conservatively estimate that they are aligned to better than 1 nm.

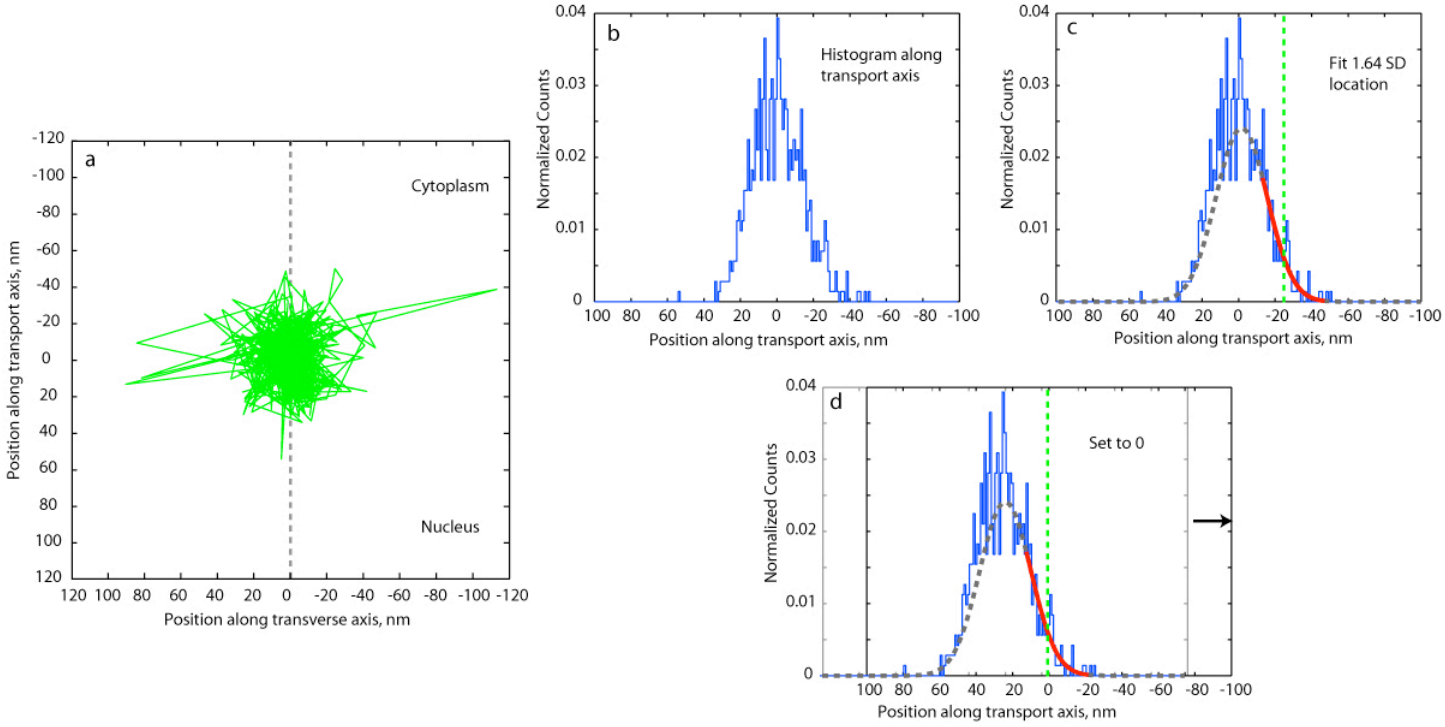

Figure S9 | Alignment of an example trajectory. (**a**) Spatial position of central channel region of single trajectory. Cytoplasm is on top, nucleus is on bottom. The dashed grey line indicates the transport axis of the NPC. (**b**) Histogram of positions along the transport axis for the same trajectory. (**c**) Histogram fit to a Gaussian distribution from 1 to 2 standard deviations (shown in red). The remainder of the Gaussian is shown in grey. The position of the 1.64 standard deviation location is determined and highlighted by the green dashed line. (**d**) The transport axis is shifted such that the zero point along the transport axis is set to the 1.64 standard deviation location. Using this scheme, 95% of the central channel region data are greater than 0.

Two-colour experiments: exploration of alternative experimental geometries to verify choice of optical geometry and alignment procedures. An alternative method for aligning trajectories is to use their position relative to the found nuclear envelope or nuclear pore complexes, but note that our ability to localise the central position of the NE is limited by diffraction to about 184 nm (= 1.22 λ / 2 NA). This limit applies when more than one emitter per diffraction volume and colour is on at any one time. There are other relevant considerations, as reported above (section 5.3). The typical difference between the NE central position as determined by brightfield vs. fluorescence is about 70 nm (Fig. S4). The reproducibility of the localization is about ± 30 nm (for brightfield images), as shown in Fig. S5b and in the table on page 5. This refers to repeated fitting of the same data, and quantifies the variation in estimates obtained from repeated runs of the bulk fitting algorithm, each starting at a different initial value.

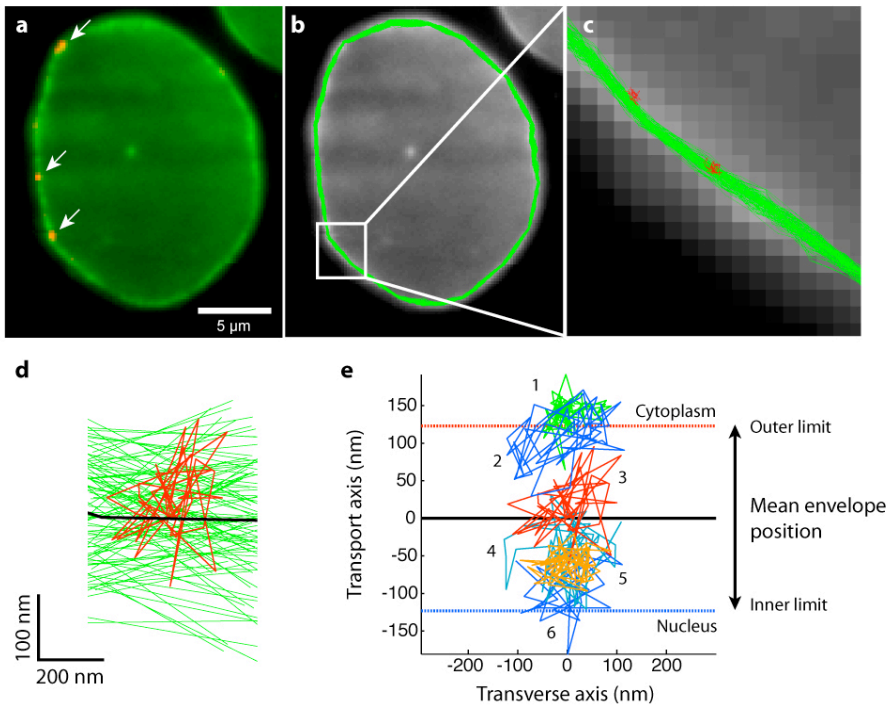

Figure S10 | Simultaneous, two colour tracking of the NE and single quantum dot cargos. (a) Average of 10 frames of a movie in which both florescence channels are being recorded simultaneously. In this particular frame three QDs (red/orange; arrows) are at the NE (as stained by importin-β-YFP; green). (b) A bundle of NE estimates. Every frame of the movie yields one estimate of the NE path (thin green line). The zoom in panel (c) shows this bundle of localizations clearly. The red signals are from single QDs. (d) As expected for localization of a signal originating from many molecules that are emitting simultaneously, there is a wide distribution of found NE estimates (green). The QD localisation precision is degraded compared to the one-colour geometry due to bleed-through and other effects that reduce the SNR and numbers of QD photons collected per frame. The black line is the mean NE position. (e) as for (d), except 6 QD tracks are plotted relative to their local mean NE position. All QD tracks are within +/- 125 nm of their mean local NE path.

Using a modified version of our instrument we simultaneously tracked the NE (as stained by importin-β-YFP) and single QD cargos. We used an Optical Insights Dualview system to split the emission by wavelength, onto the halves of one CCD chip (to enable robust temporal registration, Fig. S10).

Since the goal of this experiment was to quantify the advantages and limitations of the two-colour geometry, which we ultimately did not use, to keep things relatively simple we used the “large” QD cargos (diameter = 41±9 nm). As described in the main text, these QDs cannot easily pass the internal size gate due to their size. We also omitted RanGTP and NTF2 from the transport mix. Thus, the experiment was designed to watch single QDs encounter the constriction inside the NPC and then reside at that location for appreciable times, due to their size and the concomitant lack of NTF2/RanGTP.

The green signal in Fig. S10a comes from the importin-β-YFP, which is preferentially located within the NPC, thus delineating the NE (Fig. S10a). The other colour (red) is the signal from single QDs. The quantum dots were localised as before (section 5.1). The QD localization precision was impaired due to bleed-through from the green channel (reducing SNR) and the necessity of using a narrower QD emission filter (reducing the photon flux). We localized the NE within each frame using the importin-β-YFP signal. We fit the NE in each frame, yielding a bundle of NE localizations (Fig. 1b,c). We then plotted the QD localisation (red) on top of its local bundle of NE localisations (green, Fig. 1d). As is seen, the spread of the NE localisations is larger than the spread of the QD localisations. We then applied the same analysis to 5 more QDs (Fig. S10e). As can been seen in Fig. S10e, all QD tracks are within ± 125 nm of their mean local NE path. Thus the two-colour experimental design has advantages (such as frame-by-frame estimates of the NE location) but also reduces QD localisation precision, due to decreased SNR (green channel bleed-through) and decreased photon flux (the two-colour system contains additional lenses, mirrors, dichroics, and a narrower emission filter). We therefore used an optimised single-colour optical geometry to collect high precision data and the computational procedure described earlier in this section to align trajectories for further analysis.

6. ADDITIONAL DATA

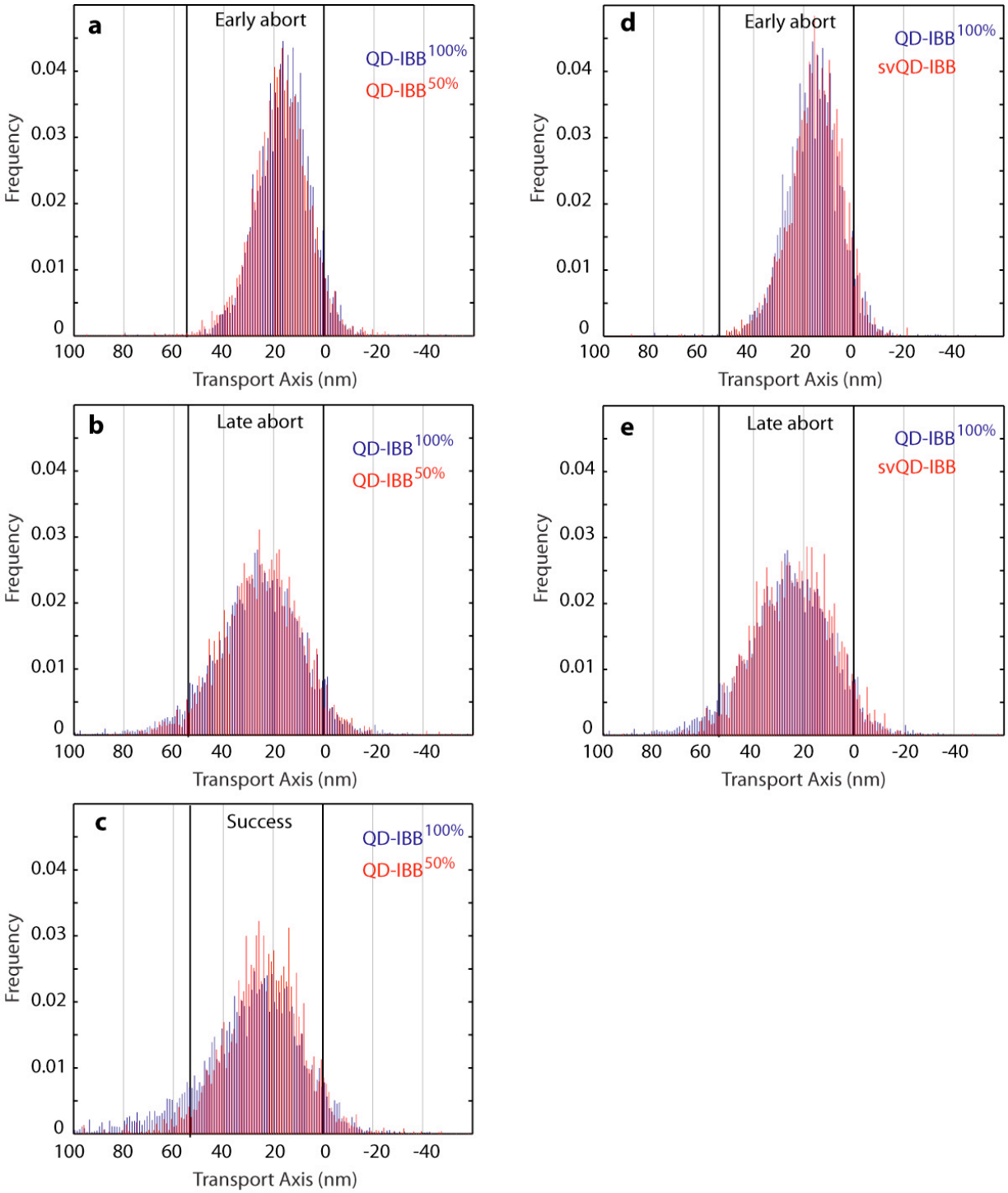

Figure S11 | Positional comparison of IBB density and Cargo size. Position histograms for QD-IBB$^{100\%}$ and QD-IBB$^{50\%}$ for (**a**) early aborts, (**b**) late aborts, and (**c**) successful trajectories. Positional histograms for QD-IBB$^{100\%}$ and larger QD-Steptavidin-IBB for (**d**) early aborts, and (**e**) late aborts. Histograms were created weighting each trajectory equally.

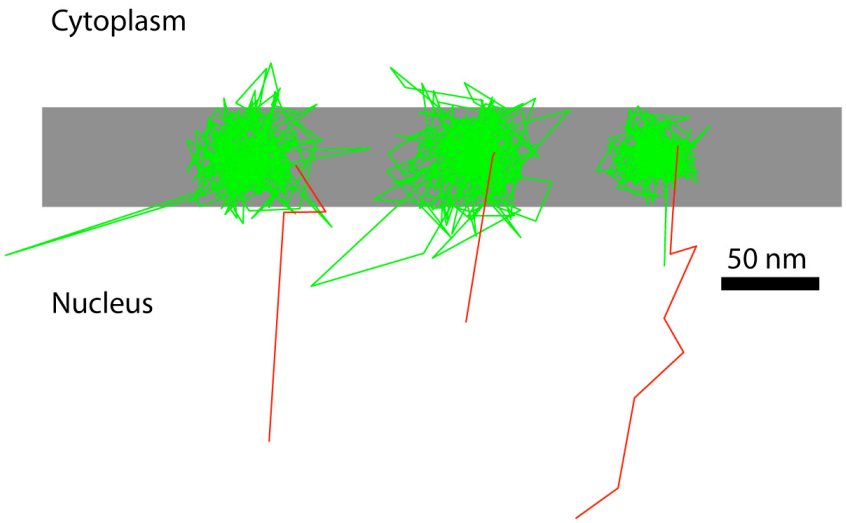

Figure S12 | Examples of successful QD cargos leaving the NPC. Trajectories of successfully importing QD cargos, with the central channel region in green and the leaving step in red. The leaving step of every trajectory in the data set is not always captured by the particle tracking, however when it is, the particle is always observed to quickly diffuse away from the NPC, leaving directly from the central channel region.

Figure S13 | Frame-to-frame displacements of cargos within the NPC. Raw frame-to-frame cargo displacements from the unfiltered 40 Hz positional data along the transverse and transport axes for late aborting (red) and successful (blue) trajectories. Error envelopes (standard error of the mean, SEM) become large at the positional extremes (> ± 20 nm in the transverse axis; beyond -10 nm to +60 nm in the transport axis) since data are extremely rare there.

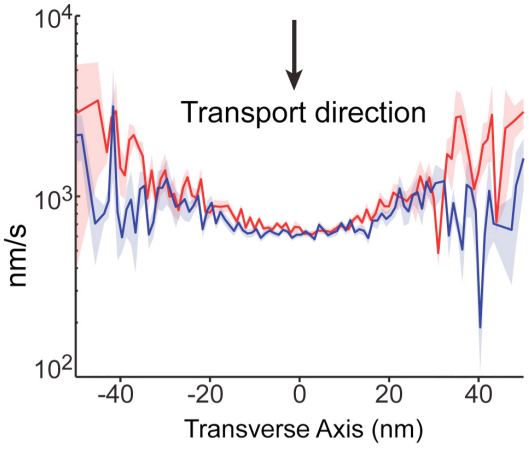

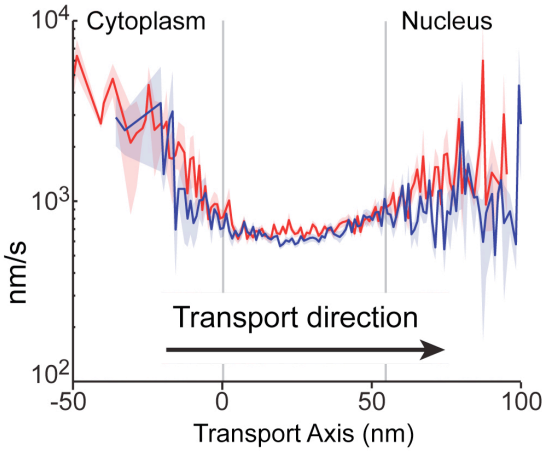

7. DATA ANALYSIS

Mean Squared Displacement (MSD). Ensemble averages of the mean squared displacement were calculated for each subset of data (early abort, late abort or success). Since the NPC is expected to be an anisotropic medium we calculated the MSD for lateral (⊥) and axial (||) motions separately. These MSD curves were then fitted to a power law ($\langle r^2 \rangle = \Gamma t^{\alpha}$), yielding the pre-factor Γ and the exponent α, summarised in Table S2 below. The fitting performed using Graphpad Prism using weighting to account for the number of data points and error in the MSD plots. Errors are standard errors.

Table S2 | Mean Squared Displacement analysis of trajectory subset.

	Early abort		Late abort		Success	
	⊥	||	⊥	||	⊥	||
Γ (m^2/s)	2.3e-16 ± 3.7e-18	2.5e-16 ± 4.3e-18	5e-16 ± 7e-18	6.3e-16 ± 8.9e-18	5e-16 ± 8e-18	6.9e-16 ± 1.2e-17
α	0.08 ± 0.01	0.13 ± 0.02	0.08 ± 0.01	0.13 ± 0.01	0.09 ± 0.01	0.19 ± 0.01

Calculation of pore crossing times. The channel crossing times were calculated for each trajectory according to the following method. First, the channel length was subdivided into three regions: (1) The cytoplasmic face, ***X*** < 10nm, (2) the channel interior 10 < ***X*** < 45 nm, and (3) the nuclear face, ***X*** > 45 nm. Next, the motion along transport axis, of each trajectory, was filtered with a 0.1s running mean filter, thus eliminating very high frequency motions (Figure 4a, blue line). Regions of this filtered trajectory were then assigned into the three regions described above (Figure 4a, red dots – cytoplasmic face, green dots – nuclear face). Crossing events were defined as those sections of the trajectory between leaving the cytoplasmic face and arriving at the nuclear face, and *vice versa*. The trend of an increase in crossing time between the QB-$IBB^{50\%}$ and QB-$IBB^{100\%}$ was also observed when the running mean filter was not employed, although the mean/median crossing times were shorter. The trend was also independent of the absolute position (within reason) of the three regions of the channel described above.

Statistical analysis of dwell and crossing times. Statistical comparisons of dwell time distributions and the crossing time distributions (Figure 4, main text) were performed using the statistical toolbox of MATLAB or Graphpad Prism. Since neither distribution is Gaussian (as confirmed by the Lilliefors test), we chose to compare the distributions using nonparametric methods. First we tested whether the two samples originated from the same underlying distribution using a two-sample Kolmogorov–Smirnov (K-S) test. Next, we compared whether the median values of the two samples were significantly different ($p < 0.05$) using the two-sided Mann-Whitney (M-W) test. The results of the tests are summarised below:

Table S3 | Statistical analyses of dwell and crossing time distributions.

	Dwell times		Crossing times	
	$IBB^{50\%}$	**$IBB^{100\%}$**	**$IBB^{50\%}$**	**$IBB^{100\%}$**
n	82	177	77	146
Mean (s)	172	122	1.43	1.29
Median (s)	94	34	0.91	0.63
p (K-S)	0.038 (p<0.05)		0.047 (p<0.05)	
p (M-W)	0.017 (p<0.05)		0.046 (p<0.05)	

1. Kalab, P., Weis, K. & Heald, R. Visualization of a Ran-GTP gradient in interphase and mitotic Xenopus egg extracts. *Science* **295**, 2452-6. (2002).
2. Askjaer, P., et al. RanGTP-regulated interactions of CRM1 with nucleoporins and a shuttling DEAD-box helicase. *Mol Cell Biol* **19**, 6276-85. (1999).
3. Mitrousis, G., Olia, A. S., Walker-Kopp, N. & Cingolani, G. Molecular basis for the recognition of snurportin 1 by importin beta. *J Biol Chem* **283**, 7877-84. (2008).
4. Cingolani, G., Petosa, C., Weis, K. & Muller, C. W. Structure of importin-beta bound to the IBB domain of importin-alpha. *Nature* **399**, 221-9. (1999).
5. Lee, S. J., Matsuura, Y., Liu, S. M. & Stewart, M. Structural basis for nuclear import complex dissociation by RanGTP. *Nature* **435**, 693-6. (2005).
6. Tokunaga, M., Imamoto, N. & Sakata-Sogawa, K. Highly inclined thin illumination enables clear single-molecule imaging in cells. *Nat Methods* **5**, 159-61. (2008).
7. Cheezum, M. K., Walker, W. F. & Guilford, W. H. Quantitative comparison of algorithms for tracking single fluorescent particles. *Biophys J* **81**, 2378-88. (2001).
8. Crocker, J. C. & Grier, D. G. Methods of digital video microscopy for colloidal studies. *J. Colloid Interface Sci.* **179**, 298-310. (1996).
9. Yang, W. & Musser, S. M. Visualizing single molecules interacting with nuclear pore complexes by narrow-field epifluorescence microscopy. *Methods* **39**, 316-28. (2006).